

Formation Mechanism and Bandgap Reduction of GaN–ZnO Solid-Solution Thin Films Fabricated by Nanolamination of Atomic Layer Deposition

Ming-Wei Liao, Horng-Tay Jeng,* and Tsong-Pyng Perng*

Nanolamination of GaN and ZnO layers by atomic layer deposition (ALD) is employed to fabricate GaN–ZnO homogenous solid-solution thin films because it offers more precise control of the stoichiometry. By varying the ALD cycle ratios of GaN:ZnO from 5:10 to 10:5, the $(\text{GaN})_{1-x}(\text{ZnO})_x$ films with $0.39 \leq x \leq 0.79$ are obtained. The formation of solid solution is explained based on the atomic stacking and preferred orientation of the layers of GaN and ZnO. However, the growth rates of GaN and ZnO during the lamination process are different from those of pure GaN and ZnO films. It is found that GaN grows faster on ZnO, whereas ZnO grows slower on GaN. The density functional theory (DFT) calculations are performed using a superlattice model for GaN and ZnO laminated layers fabricated by ALD to understand the difference of density of states (DOS) and evaluate the bandgaps for various atomic configurations in the solid-solution films. The band positions are experimentally defined by ultraviolet photoelectron spectroscopy. Significant bandgap reduction of the solid solutions is observed, which can be explained by the DOS from the DFT calculations. Visible-light-driven photocatalytic hydrogen evolution is conducted to confirm the applicability of the solid-solution films.

Compared with the fossil fuels, hydrogen possesses several advantages such as zero carbon emission, versatile production, and high energy density.^[1] Solar to hydrogen conversion by photocatalysis is sustainable and renewable without any external power. Therefore, in the past decades numerous efforts have been made to improve photocatalytic hydrogen generation efficiency. For wide bandgap semiconductor materials, they can utilize only a small fraction of solar energy. For example, anatase TiO_2 ($E_g = 3.2$ eV) can only absorb the wavelengths below 388 nm with the theoretical maximum photoconversion efficiency of 1.3% under the AM 1.5 solar spectrum.^[2] To improve the photocatalytic hydrogen evolution efficiency, the strategies of energy band engineering by doping,^[3,4] solid solution,^[5,6] and localized surface plasmon resonance^[7,8] have been adopted to achieve bandgap narrowing and visible light absorption.

1. Introduction

Hydrogen economy has been considered as one of the promising solutions for a decarbonized society in the future.

M.-W. Liao, T.-P. Perng
Department of Materials Science and Engineering
National Tsing Hua University
Hsinchu 30013, Taiwan
E-mail: tpperng@mx.nthu.edu.tw

H.-T. Jeng
Department of Physics
National Tsing Hua University
Hsinchu 30013, Taiwan
E-mail: jeng@phys.nthu.edu.tw

H.-T. Jeng
Physics Division
National Center for Theoretical Sciences
Taipei 10617, Taiwan

H.-T. Jeng
Institute of Physics
Academia Sinica
Taipei 11529, Taiwan

 The ORCID identification number(s) for the author(s) of this article can be found under <https://doi.org/10.1002/adma.202207849>.

DOI: 10.1002/adma.202207849

Li et al.^[9] reported controllable bandgaps of $\text{Zn}_{1-x}\text{Cd}_x\text{S}$ from 3.10 to 2.30 eV by increasing x from 0 to 1, achieving the visible light photocatalytic hydrogen evolution. Another approach of bandgap engineering is to alloy III–V and II–VI semiconductors.^[10] Among all the possible solid solutions, the quaternary GaP–ZnSe, GaP–ZnS, and GaN–ZnO systems exhibit abnormal bandgaps which are smaller than those of the pure component semiconductors.^[10] For example, Yang et al.^[11] fabricated $(\text{GaP})_{1-x}(\text{ZnSe})_x$ solid-solution nanowires by chemical vapor deposition (CVD). A preferred solubility in the range of $x = 0.182$ – 0.209 was obtained, resulting in varied bandgaps of 1.95–2.20 eV.^[11] Hart and Allan^[12] proposed fabrication of GaP–ZnS solid solution because both GaP and ZnS have the same zinc blende structure. Their calculation indicated that the bandgap of $(\text{GaP})_{0.875}(\text{ZnS})_{0.125}$ can be reduced to 1.9 eV with a specific ordering of the atoms. This bandgap is lower than those of bare GaP (2.24 eV) and ZnS (3.54 eV).^[12] Although the bandgaps of these two solid-solution systems have been brought down to the visible light region, they are not suitable for photocatalytic hydrogen evolution presumably owing to the corrosion susceptibility of GaP.^[13] By contrast, the GaN–ZnO system was first experimentally demonstrated to be a promising material for visible-light-driven photocatalytic hydrogen evolution by Domen's group.^[5,14,15] Since both GaN and ZnO have a hexagonal close

packed (hcp) wurtzite crystal structure, the solid solution could be homogenous and has the same structure. Although the bandgaps of GaN and ZnO are quite large, being ≈ 3.4 and ≈ 3.2 eV, respectively, it has been experimentally confirmed that the bandgap of the solid solution of GaN and ZnO could be reduced to 2.6–2.8 eV.^[15] To understand the electronic configuration, the density functional theory (DFT) calculations have been carried out using various stoichiometric and nonstoichiometric supercell models of GaN–ZnO.^[14,16–18] For example, it has been reported that from the energy state configuration the N 2p state of GaN possesses higher energy levels than those of O 2p state of ZnO. For $(\text{Ga}_{1-x}\text{Zn}_x)(\text{N}_{1-x}\text{O}_x)$ with $x = 0.42$ versus GaN, there are energy offsets of -0.3 and -1.1 eV for N 2p at the valence band edge and conduction band edge, respectively, resulting in a lower bandgap of 2.6 eV.^[16] Zhang et al. employed DFT calculations to study the stability and spatial charge distributions of 1D GaN/ZnO heterojunction with different atomic configurations, suggesting that the biaxial and superlattice heterostructure exhibits an effective bandgap decrease, especially for GaN ratios at 0.3–0.5.^[19]

Because of rapid loss of Zn in the high-temperature nitridation process, it is hard to precisely control the Ga:Zn ratio and fabricate ZnO-rich solid solutions by nitridation of the mixture of ZnO and Ga_2O_3 powders. Tongying et al. solved this problem by using the nanocrystals of ZnO and ZnGa_2O_4 as the starting materials.^[20] They successfully synthesized the solid solutions of $(\text{Ga}_{1-x}\text{Zn}_x)(\text{N}_{1-x}\text{O}_x)$ with $x = 0.21$ to 0.87. On the other hand, Yang et al. demonstrated the fabrication of $(\text{Ga}_{1-x}\text{Zn}_x)(\text{N}_{1-x}\text{O}_x)$ solid-solution films by using pulse laser deposition with a multitarget, obtaining the lowest optical bandgap of ≈ 2.0 eV at $x = 0.65$.^[21] While these investigations have provided some feasible solutions for composition control of the solid solution, none of the studies has employed the fabrication method of atomic layer deposition (ALD) that can control the composition more precisely.

As a promising photocatalyst, the fabrication of ZnO-based films and nanostructures has been widely investigated by several techniques including sol–gel, in situ self-assembly, electrospinning, thermal decomposition, and other hydrothermal and microwave-assisted methods.^[22] These solution-based methods provide the advantages of low cost and controllable morphology but usually need a posttreatment at a relatively high temperature of 300–600 °C to form crystalline and homogenous ZnO nanocomposites.^[22,23] On the other hand, CVD and ALD are commonly used for fabrication of GaN/ZnO heterojunction film as the light-emitting diodes.^[24,25] Despite longer process time of ALD, highly crystalline ZnO films with a surface roughness of only 1–4 nm can be formed on Si wafer, especially at a low temperature of 90–200 °C.^[26] It is thus that ALD possesses a high potential to fabricate GaN–ZnO solid solution. The relatively low fabrication temperature can also suppress oxidation of GaN or formation of ZnGa_2O_4 .

In our previous work, the nanolamination of ALD has been applied to fabricate solid solutions of ZnO-TiO_2 and $\text{Al}_2\text{O}_3\text{-TiO}_2$, as well as $\text{Al}_2\text{O}_3\text{-ZnO}$.^[27–29] Nanolaminates manufactured by ALD possess several advantages including excellent film conformity, stoichiometry flexibility, and thickness controllability.^[30] Accordingly, in the present study, ALD nanolamination was employed to fabricate the GaN–ZnO solid-solution films by varying the cycle ratio of Ga and Zn precursors. For the growth

of GaN, the ALD window of trimethyl gallium (TMG) is typically at above 450 °C, but it has been proven to be self-limiting at 185–385 °C using NH_3 plasma with a saturation time of 90 s.^[31] The self-limiting growth of ZnO has been reported to occur at 200–260 °C using diethyl zinc (DEZ) and H_2O as the precursors.^[32] Based on these conditions, the ALD nanolamination process can be conducted at a relatively low temperature of 200 °C. The effects of ALD cycle ratio on the composition and crystallization characteristics were examined. In addition, the DFT calculations were performed using a superlattice model for GaN and ZnO to evaluate the bandgap and understand the difference of density of states (DOS) for various atomic configurations of the solid-solution thin films.

2. Characterization Results

2.1. Structural Characteristics of the Films

Figure S1 in the Supporting Information shows the thicknesses of pure GaN and ZnO deposited on Si by various cycles of ALD using the optimized precursors and reactant exposure time. A perfect linear relationship between the thickness and cycle number was observed for both films, confirming self-limiting growth at 200 °C. The growth rates for GaN and ZnO were calculated to be 0.8 and 2.0 Å per cycle, respectively.

Figure 1 shows the grazing-incidence X-ray diffraction (GIXRD) patterns of the as-deposited GaN–ZnO thin films fabricated by ALD nanolamination with various cycles of GaN and ZnO. Note that the numbers represent the deposition cycle ratios. For example, G5Z10 consists of a repetition of five cycles of GaN and then ten cycles of ZnO. A total of 300 ALD cycles were performed for each film. For comparison, the bare GaN and ZnO thin films formed by ALD are also shown. Since both GaN and ZnO belong to an identical hexagonal wurtzite structure but with slightly different lattice constants, the peak positions of three major diffraction peaks are very close. The as-deposited GaN thin film shows an amorphous structure. By contrast, the as-deposited ZnO thin film is well crystallized and the three diffraction peaks can be indexed to the (100), (002), and (101) planes from the powder diffraction file (PDF, #00-036-1451). The peak positions from the PDF database for GaN and ZnO are indicated as dashed lines in Figure 1. By varying the ALD cycle ratio of GaN:ZnO from 5:10 to 5:5 (denoted as G5Z10 and G5Z5, respectively), it is clearly observed that the (100) diffraction peak, e.g., shifts to a higher angle between those of the standard ZnO and GaN positions, as shown in Figure 1. Table 1 lists the precise values of all peak positions and the corresponding lattice parameters, which reveals that all the peak positions of (100), (002), and (101) diffraction peaks move toward higher angles with the following order: ZnO, G5Z10, G5Z7, and G5Z5. Compared to G5Z5, the (100) peak position of G7Z5 is further increased, but the (002) and (101) peak positions are slightly decreased to lower angles. The peak shift from ZnO to GaN as the ALD cycle ratio of GaN:ZnO increases implies that homogenous GaN–ZnO solid solutions were formed by ALD nanolamination. That is, despite the bare GaN is amorphous, formation of a crystalline phase was achieved with the aid of crystalline ZnO interlayers.

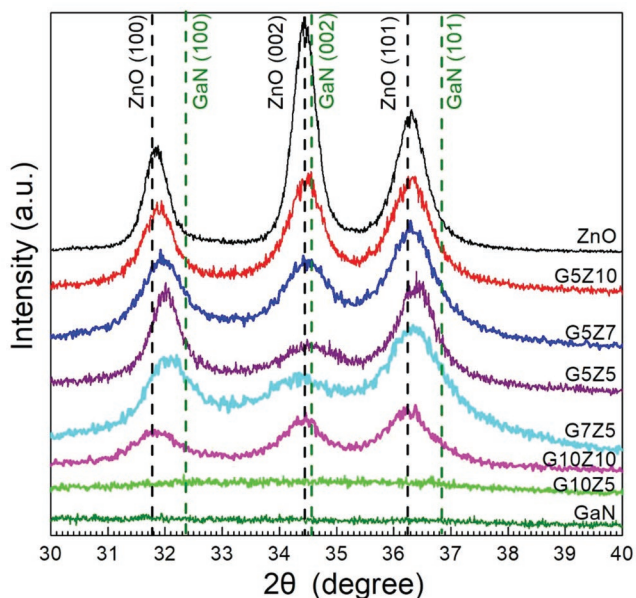


Figure 1. GIXRD patterns of as-deposited GaN–ZnO thin films fabricated by ALD nanolamination with various cycles of GaN and ZnO. Diffraction positions of GaN and ZnO indicated by green and black dashed lines are referred to PDF databases #00-050-0792 and #00-036-1451, respectively.

On the other hand, it is seen that G10Z10 exhibits more broadened peaks with lower intensity, and the peak positions are almost the same as those of ZnO. Furthermore, G10Z5 reveals no diffraction peaks, similar to pure GaN. It implies that increasing the ALD cycles of GaN from 5 to 10 is unfavorable for formation of crystalline thin film. It is worthy of comparing the features of G5Z5 and G10Z10. Both samples possess identical ratio and total ALD cycles of GaN and ZnO, yet the latter shows much worse crystallinity. The probable reason is that a thick amorphous GaN interlayer would hinder the formation of a uniform solid solution. For G10Z5, the growth behavior might be overwhelmed by that of amorphous GaN.

In order to further investigate the microstructure of GaN–ZnO thin films, all of the diffraction patterns except G10Z5 and GaN are deconvoluted to lorentzian peaks for the lattice planes of (100), (002), and (101) to estimate the peak intensity of each individual plane. The values are also shown in Table 1. Interest-

ingly, it is observed that the as-deposited ZnO shows a much stronger intensity of the (002) plane than those of the (100) and (101) planes. In contrast, the G5Z5 solid-solution film shows a lower intensity of the (002) plane than those of the (100) and (101) planes. Therefore, to quantify the preferred orientations of the ZnO and GaN–ZnO thin films, Harris's method^[33] was performed to calculate the texture coefficient (TC) for each (*hkl*) plane by the following equation

$$TC(hkl) = \frac{I(hkl)}{I_0(hkl)} / \frac{1}{N} \sum_N \frac{I(hkl)}{I_0(hkl)} \quad (1)$$

where $I(hkl)$ is the intensity of the diffraction peak (*hkl*), $I_0(hkl)$ is the relative intensity of the (*hkl*) of ZnO obtained from the literature database (PDF#00-036-1451), and N is the number of diffraction peaks to be considered. For the hexagonal wurtzite ZnO, $N = 3$ was chosen to estimate the three major peaks of (100), (002), and (101). Therefore, the value of TC would be equal to 1 for a standard ZnO sample without any preferred orientation.

In the present experiment, the ZnO thin film possesses a high TC(002) value of 1.90, indicating a very strong preferred orientation along the *c*-axis which is perpendicular to the substrate. However, when GaN was incorporated into the films, the value of TC(002) dramatically decreased but the values of TC(100) and TC(101) increased with increasing the ALD cycle ratio of GaN:ZnO from 5:10 to 5:5. For the G5Z5 sample, the value of TC(100) is estimated to be 1.37, larger than those of TC(002) and TC(101), indicating that increasing the ratio of GaN layers facilitated the growth of GaN–ZnO thin film along the *a*-axis rather than along the *c*-axis. In addition, it is worthy of mentioning that both G5Z10 and G10Z10 possess very similar values of TC(*hkl*), implying that the number of continuous ALD cycles of ZnO in the laminate is a major factor to affect the overall crystal growth behavior.

To further verify the effect of ALD cycle ratio on the thin-film growth behavior, the crystallite size of each sample was estimated by Debye–Scherer formula as follows

$$D = \frac{K\lambda}{\beta \cos \theta} \quad (2)$$

where D is the crystallite size, K is the shape factor (typically $K = 0.9$), λ is the X-ray wavelength, β is full-width at half-maximum (FWHM) of the peak, and θ is the Bragg angle.

Table 1. Values of 2θ , lattice parameters, intensity, and texture coefficient for different GaN–ZnO thin films from the GIXRD patterns.

Sample	2θ [degree]			Lattice constant [Å]		Intensity [a.u.]			Texture coefficient		
	(100)	(002)	(101)	<i>a</i>	<i>c</i>	(100)	(002)	(101)	(100)	(002)	(101)
ZnO(PDF#036-1451)	31.77	34.42	36.25	3.249	5.206	570	440	1000	–	–	–
ZnO	31.84	34.44	36.29	3.242	5.204	315	750	437	0.62	1.90	0.49
G5Z10	31.88	34.45	36.30	3.239	5.202	279	376	374	0.85	1.49	0.65
G5Z7	31.94	34.46	36.32	3.233	5.202	246	242	334	0.98	1.25	0.76
G5Z5	32.01	34.49	36.39	3.226	5.196	334	150	356	1.37	0.80	0.83
G7Z5	32.05	34.35	36.36	3.222	5.218	223	155	309	1.12	1.01	0.88
G10Z10	31.84	34.39	36.29	3.242	5.212	105	142	167	0.82	1.44	0.74
GaN (PDF#050-0792)	32.39	34.56	36.85	3.189	5.185	560	450	1000	–	–	–

Table 2. Values of FWHM, crystallite size, microstrain, and dislocation density for different GaN–ZnO thin films derived from the GIXRD patterns.

Sample	FWHM [°]			Crystallite size [nm]			Microstrain [10 ⁻³]			Dislocation density [10 ¹⁵ lines m ⁻²]		
	(100)	(002)	(101)	(100)	(002)	(101)	(100)	(002)	(101)	(100)	(002)	(101)
ZnO	0.44	0.45	0.62	18.8	18.6	13.5	6.7	6.3	8.2	2.8	2.9	5.4
G5Z10	0.71	0.74	0.83	11.5	11.2	10.1	10.9	10.4	11.0	7.4	7.9	9.7
G5Z7	1.02	1.06	1.01	8.1	7.8	8.2	15.6	14.9	13.4	15.2	16.2	14.6
G5Z5	0.68	1.51	0.80	12.1	5.5	10.5	10.4	21.2	10.6	6.8	32.9	9.0
G7Z5	1.15	1.87	1.35	7.1	4.4	6.1	16.5	24.2	19.6	17.3	42.6	31.0
G10Z10	1.25	0.93	1.02	6.6	8.9	8.1	19.2	13.0	13.6	23.0	12.4	15.0

The FWHM was obtained by lorentzian fitting. The calculated values of FWHM and crystallite size are shown in Table 2. It can be found that the bare ZnO thin film reveals similar crystallite sizes of 18.88 and 18.61 nm along the specific crystallographic directions perpendicular to (100) and (002), respectively, but a smaller crystallite size of 13.55 nm along the direction perpendicular to (101). For G5Z10 and G5Z7, the crystallite sizes along the three directions are very close to each other despite their stronger preferred orientation of (002). Generally, it is observed that the crystallite size tends to decrease with reducing the ZnO cycle ratio or raising the GaN cycle ratio. For example, G10Z10 shows much decreased crystallite sizes in each direction compared to those of G5Z10. In addition, it is also noted that G5Z5 and G7Z5 possess significantly larger crystallite size along the direction perpendicular to (100) than those perpendicular to (002), which has the same variation trend as that of TC. These results suggest that GaN tends to crystallize on the ZnO (100) plane, resulting in a larger crystallite size of solid solution along the direction perpendicular to (100). However, the crystallite sizes of G7Z5 along the three directions are much smaller than those of G5Z5, presumably due to a thicker amorphous GaN layer. Furthermore, the crystallite sizes of G7Z5 along the directions perpendicular to the (002) and (101) planes are as small as 4.4 and 6.1 nm, respectively. As previously mentioned, the (002) and (101) peak positions of G7Z5 are abnormally decreased to lower angles than those of G5Z5. Therefore, the low-angle shift of (002) and (101) would be attributed to the defect-induced internal stress due to more amount of amorphous GaN.

In addition to the crystallite size, the microstrain (ϵ) and dislocation density (δ) were calculated by the following equations^[34,35]

$$\epsilon = \frac{\beta}{4 \tan \theta} \quad (3)$$

$$\delta = \frac{1}{D^2} \quad (4)$$

The calculated results are also shown in Table 2. The fact that the microstrain and dislocation density increase with decreasing the ZnO cycle ratio from G5Z10 to G5Z7 or increasing the GaN cycle ratio from G5Z5 to G7Z5 can be attributed to more stacking faults between GaN and ZnO. It is also noticed that the significantly large microstrain and dislocation density occur on the (002) and (101) planes of G7Z5, implying more linear defects formed on these two planes. Again, this might be consistent with the abnormal low-angle shift of these two planes in the XRD pattern, Figure 1.

Figure S2 in the Supporting Information shows 3D atomic force microscopy (AFM) morphologies of ZnO, GaN, and various GaN–ZnO solid-solution films. It is observed that the bare ZnO film possesses a much rougher surface with Ra = 4.03 nm presumably owing to the largest crystallite size and strong (002) preferred orientation. By contrast, the bare GaN film exhibits a flatter surface with Ra = 0.88 nm because of its amorphous structure. For GaN–ZnO solid-solution films, it is observed that for G5Z5, G5Z7, and G5Z10, the roughness appears to increase as the ZnO cycle number increases. This could be ascribed to the intrinsic behavior of crystalline ZnO. When the cycle number of ZnO is fixed, however, the roughness also increases as the amount of GaN increases, i.e., G10Z5 (Ra = 2.88 nm) > G7Z5 (Ra = 1.95 nm) > G5Z5 (Ra = 1.58 nm). Also, G10Z10 possesses a rougher surface (Ra = 1.99 nm) than that of G5Z5. It might be caused by the larger strain induced by more layers of GaN, as evidenced by the values shown in Table 2. Therefore, the morphologies of the films may be controlled by multifactors associated with the intrinsic characteristics of ZnO and GaN films as well as the interfacial mismatch between the two compounds.

2.2. Atomic Stacking in the Solid Solutions

According to the characteristics of texture coefficients and crystallite sizes of the various GaN–ZnO solid-solution films, the schematic atomic configurations and crystal growth diagrams for three films during ALD nanolamination are illustrated in Figure 2. For G5Z5 with the GaN:ZnO cycle ratio of 5:5,

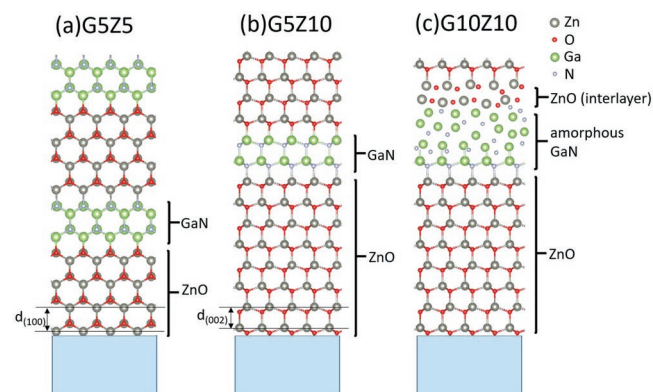


Figure 2. a–c) Schematic diagrams of ALD nanolamination for G5Z5 (a), G5Z10 (b), and G10Z10 (c).

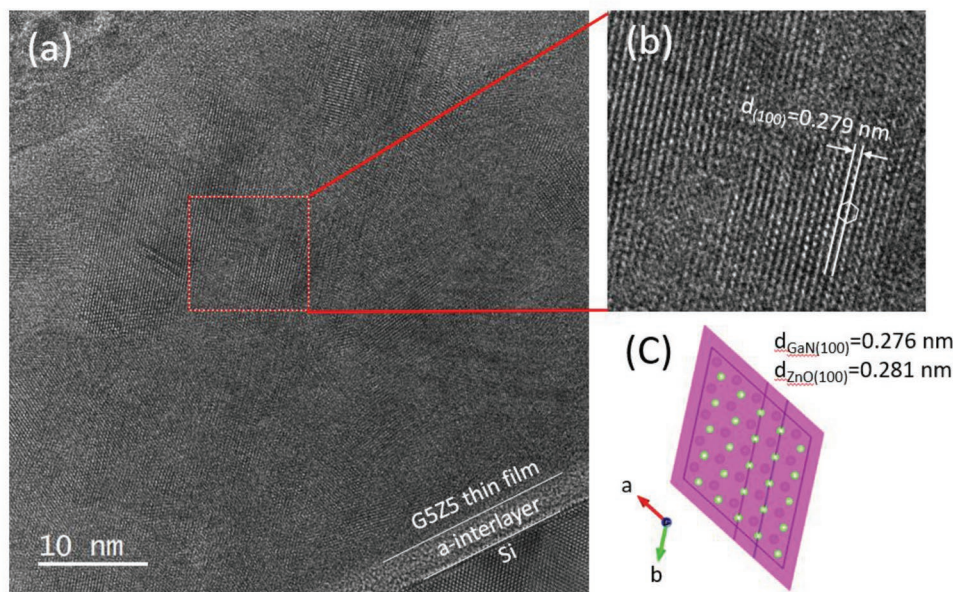


Figure 3. a) Cross-sectional HRTEM image of the G5Z5 thin film, b) enlarged HRTEM image, and c) schematic hexagonal wurtzite atomic arrangement on the (001) facet.

approximately four atomic layers of ZnO and two atomic layers of GaN are alternately stacked on the preferred (100) plane during the ALD process (Figure 2a). In contrast, for G5Z10 with a longer growth period for stacking ZnO, it possesses eight layers of ZnO and two layers of GaN, but on the preferred (002) plane (Figure 2b). In these two configurations, two layers of GaN can be bonded coherently with the intrinsic wurtzite ZnO crystal to form a solid solution. On the other hand, when increasing the cycle ratio of GaN from 5 to 10, i.e., G10Z10, although also on the preferred (002) plane of the initial ZnO layers, the following deposition of four layers of amorphous GaN results in confusion in the subsequent stacking of ZnO (Figure 2c), leading to decrease of overall crystallite size in G10Z10.

Figure 3a shows a cross-sectional high-resolution transmission electron microscopic (HRTEM) image of the G5Z5 thin film. It clearly reveals that the film with a homogenous polycrystalline microstructure is deposited on the Si substrate. Moreover, a well-crystallized hexagonal atomic arrangement with a lattice spacing of 0.279 nm can be observed, as shown in the enlarged image (Figure 3b). Referring to the wurtzite structure and lattice parameters, the hexagonal atomic arrangement and lattice distance can be well defined as the (001) facet and the *d*-spacing of (100), respectively, as shown in Figure 3c. Therefore, the TEM image suggests that the atomic stacking is along the directions of *a* and *b* axes during the ALD process, which is in good agreement with the XRD measurements. Based on the PDF database, the (100) *d*-spacings of GaN and ZnO are 0.276 and 0.281 nm, respectively. The lattice spacing of 0.279 nm observed in Figure 3b is attributed to the formation of a solid solution of GaN and ZnO.

Figure 4 shows the energy-dispersive X-ray (EDX) mappings for the G5Z5 thin film in the cross-sectional view of TEM. Despite the Si substrate and amorphous interlayer at the right corner of the bottom shown in Figure 4a, the elemental

mappings (Figure 4b,e) show that Ga, N, Zn, and O elements are homogeneously distributed in the entire G5Z5 film without any segregation. It is also observed that the amorphous interlayer contains N and O atoms without Ga and Zn, implying that silicon oxynitride was formed in the initial ALD cycles of H₂O and NH₃. The EDX mapping results suggest that the GaN–ZnO thin film prepared by ALD nanolamination can be considered as a solid solution rather than a composite.

Figure 5 shows the X-ray photoelectron spectroscopic (XPS) spectra of Zn 2p 3/2 and Ga 3d for GaN, ZnO, and all GaN–ZnO solid-solution films. The binding energies are charge corrected using the C 1s binding energy of 284.6 eV as a reference. The pure ZnO film as well as other solid-solution films show the XPS peaks of Zn 2p 3/2 at the same binding energy of 1021.7 eV, which represents the typical Zn–O bond and is in agreement with those reported for bulk ZnO^[36] and ZnO film.^[37] While for the Ga 3d, it is observed that the peaks exhibit various chemical shifts depending on the film compositions. First, the pure GaN and G10Z5 film exhibit the Ga 3d peaks at 20.3 eV which is corresponding to the Ga–N bond,^[38] confirming the formation of amorphous G10Z5. Second, the peaks are shifted to a slightly lower binding energy of 20.0 eV for G7Z5, G5Z5, G5Z7, and G5Z10. Third, the G10Z10 sample exhibits a larger shift to 19.6 eV. Although to the best of our knowledge none of the studies has reported the chemical shift of GaN–ZnO solid solution, the similar chemical shift toward lower energy has been observed in GaN incorporated with Mg.^[39] The peak position of Ga 3d was shifted from 20.38 to 19.85 eV with increasing the Mg:Ga ratio from 0 to 0.1102.^[39] Therefore, the chemical shift of Ga 3d peaks implies the formation of solid solution with ZnO, and the larger shift of G10Z10 can be referred to the different characteristic of its XRD pattern.

Table 3 lists the chemical compositions of the GaN–ZnO solid-solution films obtained by the XPS analysis, x , and

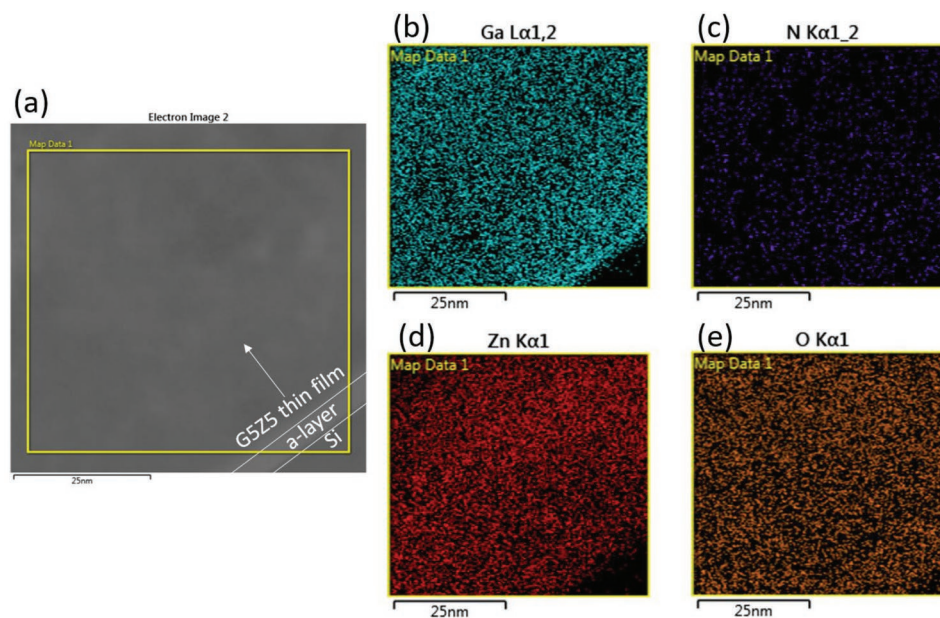


Figure 4. EDX-TEM elemental mappings of the G5Z5 thin film. a) Cross-sectional TEM image, and b–e) elemental mappings of Ga, N, Zn, and O, respectively.

calculation based on the growth rates, x' . As the individual ALD growth rates per cycle of GaN and ZnO are ≈ 0.8 and ≈ 2.0 Å, respectively, the ideal values of x' for GaN–ZnO solid-solution films can be calculated based on the densities and atomic weights of the individual GaN and ZnO films. The real mass densities of bare GaN and ZnO films were retrieved from the X-ray reflectivity (XRR) measurement to be 4.41 and 5.53 g cm $^{-3}$, respectively. The measured density of ZnO film is close to that of bulk ZnO, 5.61 g cm $^{-3}$. However, the density of GaN film is lower than that of bulk GaN (6.15 g cm $^{-3}$), which is probably due to the structural defects and residual carbon.^[40] The experimental data can be quantified by the relative sensitivity factor (RSF)^[41] modified peak areas of Ga 3d and Zn 2p in the XPS spectra. Based on the values of RSF, also shown in Table 3, the values of x in (GaN) $_{1-x}$ (ZnO) $_x$ experimentally determined by XPS for G5Z5, G5Z7, G5Z10, G7Z5, G10Z5, and G10Z10 are derived to be 0.66, 0.75, 0.79, 0.52, 0.39, and 0.68, respectively. These values are all lower than those ideal values x' calculated from the individual growth rates of bare GaN and ZnO, and the differences between x and x' are especially larger for G10Z5 and G7Z5 with higher cycle ratios of GaN:ZnO. This implies that the growth rates of GaN and ZnO in the solid-solution films are not the same as those of bare GaN and ZnO. Therefore, the actual growth behaviors during the lamination process would require further investigation.

Figure 6a shows the dependence of film thickness (measured by XRR and ellipsometry) on the ALD cycles of GaN and ZnO. It is found that the actual thicknesses of G10Z5, G7Z5, G5Z5, and G10Z10 are smaller than the theoretical values calculated by the individual growth rates of GaN and ZnO, implying that the growth rates of ZnO during the ALD lamination process in these samples are lower than that of pure ZnO (2.0 Å per cycle). As discussed above, the amorphous GaN layer may cause a different growth mechanism. **Figure 6b** shows the dependence

of real mass density (measured by XRR) on the ALD cycles of GaN and ZnO. Note that the theoretical curve is calculated based on the individual growth rates and real densities of bare GaN and ZnO films. The true densities of the GaN–ZnO solid-solution films from the experiment, except G5Z7, are lower than the ideal values, implying higher growth rates of GaN in these samples during the ALD lamination process. Based on the thicknesses experimentally measured by XRR and ellipsometry and the chemical compositions of x determined by XPS, it can be calibrated that the actual growth rates during the lamination process of GaN/ZnO for G10Z5, G7Z5, G5Z5, G10Z10, G5Z7, and G5Z10 are $\approx 0.9/\approx 0.9$, $\approx 1.0/\approx 1.1$, $\approx 1.0/\approx 1.6$, $\approx 1.0/\approx 1.6$, $\approx 1.1/\approx 1.8$, and $\approx 1.2/\approx 1.8$ Å per cycle, respectively, as shown in **Figure 6c**. Note that these calibrated growth rates can well match with the aforementioned measured thicknesses. The variation of growth rate in different solid-solution films may be ascribed to different nucleation sites on different substrates.^[42] Therefore, the significantly decreased growth rates of ZnO in G10Z5 and G7Z5 are attributed to the nucleation delay of ZnO on amorphous GaN. On the other hand, the increased growth rates of GaN in G5Z7 or G5Z10 imply that GaN can nucleate more easily on ZnO with a crystalline wurtzite structure. With this calibration of the growth rates, the stoichiometry of the GaN–ZnO solid solution can be controlled by varying the ALD lamination layers.

Figure S3 in the Supporting Information shows the thicknesses of G5Z5 films deposited on Si with various cycles of ALD. It demonstrates that a linear dependence between the thickness and cycle number can be achieved with the lamination process. Based on the above calibrated actual growth rates for G5Z5, $\approx 1.0/\approx 1.6$ Å per cycle, the thicknesses for total cycle numbers of 50, 100, 150, and 300 would be 6.5, 13.0, 19.5, and 39.0 nm, respectively. These values are consistent with those obtained by the experiment.

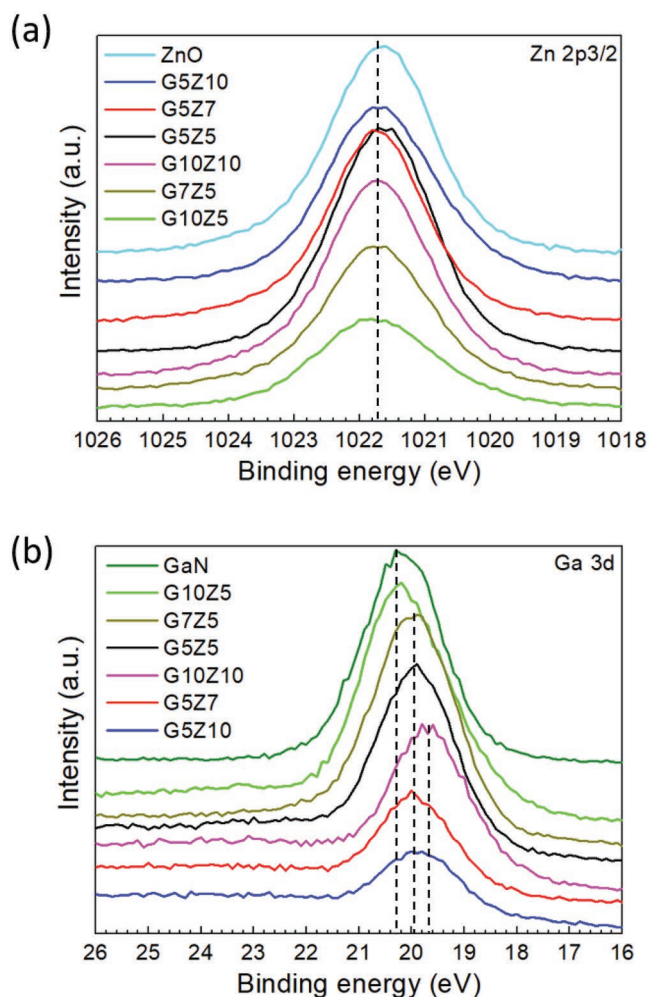


Figure 5. a,b) XPS spectra of Zn 2p 3/2 (a) and Ga 3d (b) for pure ZnO, GaN, and various GaN-ZnO solid-solution films.

3. DFT Calculations and the Band Energies

Figure 7 presents the values of total DOS (TDOS) of GaN, ZnO, and G5Z5 samples by DFT calculations based on a 48-atom supercell model. From the XPS results and preferred orientations of atomic stacking, a 48-atom superlattice model with four atomic layers of ZnO and two atomic layers of GaN along the *a*-axis was established to describe ALD nanolamination of GaN

Table 3. Relative sensitivity factors and chemical compositions of the GaN-ZnO thin films from the XPS analysis and growth rates.

Sample	Zn 2p (RSF area)	Ga 3d (RSF area)	GaN _(1-x) ZnO _(x)	
			<i>x</i> , XPS	<i>x'</i> , ideal
G5Z5	590.1	302.4	0.66	0.76
G5Z7	508.1	171.0	0.75	0.81
G5Z10	491.7	130.0	0.79	0.86
G7Z5	411.1	375.1	0.52	0.69
G10Z5	261.7	410.2	0.39	0.61
G10Z10	551.8	259.0	0.68	0.76

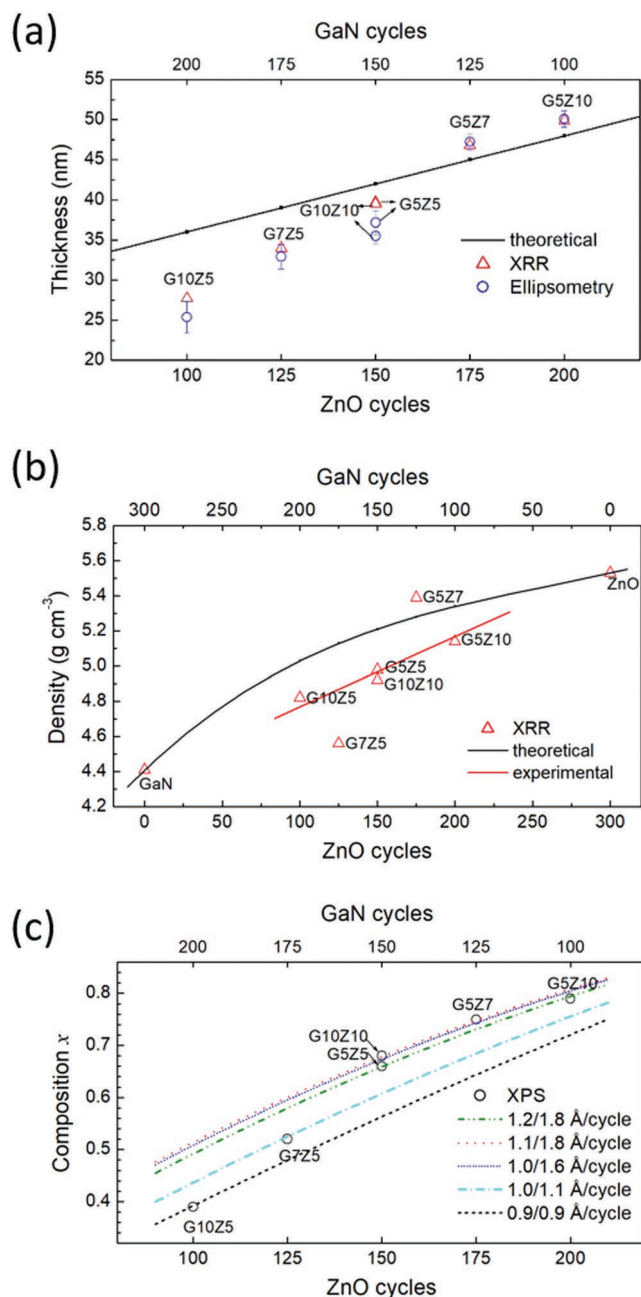


Figure 6. a–c) Dependence of film thickness (a), mass density (b), and composition (c) on ALD cycles of GaN and ZnO. The theoretical curves in (a) and (b) are obtained based on the growth rates and densities of individual films of GaN and ZnO.

and ZnO in G5Z5, as shown in Figure 7a. Since the forbidden energy gaps are always underestimated for materials containing electrons from the d orbital, a Coulomb repulsion energy *U* was introduced into the DFT calculations to improve insufficient description of the electrons, as known as DFT+*U*.^[43] From the DOS with alignment of the Fermi level to 0 eV, it is clearly observed that G5Z5 possesses a narrowed bandgap compared to those of GaN and ZnO, as shown in Figure 7b. The onset values of the conduction band minimum (CBM) are 1.54, 2.49, and 2.19 eV for G5Z5, GaN, and ZnO, respectively. Although

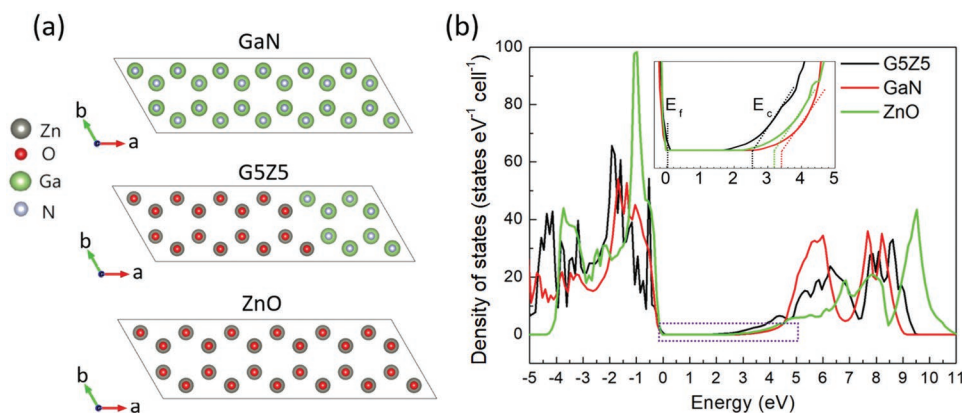


Figure 7. a) 48-atom supercell models of GaN, ZnO, and G5Z5 for DFT calculations. b) TDOS of GaN, ZnO, and G5Z5. The inset shows an enlarged portion of 0 to 5 eV with the cut-off energy as the modified CBM.

the above values still seem to be underestimated compared to other experimental data,^[14–20] it was found that the CBM edges determined by the cut-off method are well matched to the experimental data of GaN (3.4 eV) and ZnO (3.2 eV), as shown in the inset of Figure 5b. Therefore, the calculated bandgap of G5Z5 can be modified to be 2.56 eV which is a reasonable value compared with those from previous reports^[20,44,45] and our measured optical bandgap of 2.66 eV, as shown in Figure S4 in the Supporting Information.

Considering the presence of microstrain and defects might affect the DOS, additional calculations were carried out. Figure S5 in the Supporting Information presents the variation of TDOS of G5Z5 with $\pm 0.25\%$ strain (i.e., with different lattice constants) and doping with one and two electrons. Compared to original G5Z5, although the overall curves of DOS with $\pm 0.25\%$ strain are slightly modified, there is essentially no change of bandgap, as shown in Figure S5a in the Supporting Information. In addition, since ZnO is naturally an n-type semiconductor due to the intrinsic defect of oxygen vacancies,^[46] the electron doping was applied in the DFT calculations to simulate the presence of additional electrons. As shown in Figure S5b in the Supporting Information, the major variation of DOS occurs in lower energy levels of the valence band and higher energy levels of the conduction band. Again, the bandgap is basically unchanged. Therefore, the CBM edges would not change in crystalline G5Z5 with low defect densities.

The values of partial density of states (PDOS) projected on the Zn, O, Ga, and N atoms for all GaN–ZnO solid-solution films were calculated using the atomic configurations based on the chemical compositions obtained from the XPS analysis, as shown in Figure 8a. The ratio of ZnO:GaN in these primitive cells of $(\text{GaN})_{1-x}(\text{ZnO})_x$ might be slightly different from the experimental values x due to the necessity of integer number of atoms in the cell. For example, 32 Zn/O and 8 Ga/N atoms, i.e., the ratio of ZnO is 0.80, are assigned for the model of G5Z10 in which the experimental value of x is 0.79. For the models of G7Z5 and G10Z5, the numbers of Zn atoms decrease to 12 and 9, respectively, in order to match with the results of the XPS analysis.

For the 48-atom primitive cells (G5Z5, G5Z7, and G5Z10), the values of PDOS projected on Ga and N atoms increase

in the region near the valence band maximum (VBM) edge (around -3 to 0 eV) and those on Zn and O atoms decrease in the region near the CBM edge (around 2 – 5 eV) when x is reduced from 0.66 (G5Z5) to 0.39 (G10Z5), as shown in Figure 8b. The values of DOS in the CBM edge follow the order $\text{G5Z5} > \text{G7Z5} > \text{G10Z5}$, implying that a higher content of ZnO is necessary to obtain more DOS in the conduction band and smaller bandgap. For the primitive cells of G5Z5, G5Z7, and G5Z10, with increasing the numbers of Zn and O atoms but an identical number of Ga and N atoms, it is observed that the PDOS projected on Ga and N atoms decrease in the region near the VBM edge and those on Zn and O atoms increase in the region near the CBM edge when x is increased from 0.66 (G5Z5) to 0.79 (G5Z10). This behavior is the same as that for the series of G5Z5, G7Z5, and G10Z5 primitive cells. As for the primitive cell of G10Z10, the size can be seen as two times of the primitive cell of G5Z5. It reveals that the values of PDOS are approximately twice more than those of G5Z5.

From the calculated values of DOS, the modified bandgaps of $(\text{GaN})_{1-x}(\text{ZnO})_x$ are 2.67, 2.61, 2.56, 2.55, 2.34, and 2.19 eV for G10Z5 ($x = 0.39$), G7Z5 ($x = 0.52$), G5Z5 ($x = 0.66$), G10Z10 ($x = 0.68$), G5Z7 ($x = 0.75$), and G5Z10 ($x = 0.79$), respectively. Notice that the modified bandgaps for G5Z5 and G5Z10 are basically the same, i.e., 2.56 and 2.55 eV, respectively. These results suggest that the bandgap would be reduced when increasing the ratio of ZnO. The values of PDOS further reveal that the narrowed bandgaps are primarily attributed to the Zn and O states in the CBM and the Ga and N states in the VBM, which is consistent with the general band structures of ZnO and GaN.^[16]

Ultraviolet photoelectron spectroscopic (UPS) analysis was performed to determine the work functions (Φ) and valence band edges. Figure 9 shows the UPS and UPS-valence band (UPS-VB) spectra for the bare GaN, bare ZnO, and all GaN–ZnO samples. The work function can be determined by the cut-off energy (E_{cut}) and onset energy (E_{onset}) in the UPS spectra with the equation $\Phi = h\nu$ (21.22 eV) $- E_{\text{cut}} + E_{\text{onset}}$. From the UPS spectra, the values of Φ of GaN and ZnO were estimated to be 4.03 and 4.85 eV, respectively. Moreover, the onset in the UPS-VB spectra indicates the energy difference ($E_{\text{V-F}}$) between the valence band edge (E_{VB}) and the Fermi level (E_{F}). The values of E_{cut} , E_{onset} , Φ , $E_{\text{V-F}}$, E_{VB} , and the bandgap (E_{g}) from the DFT

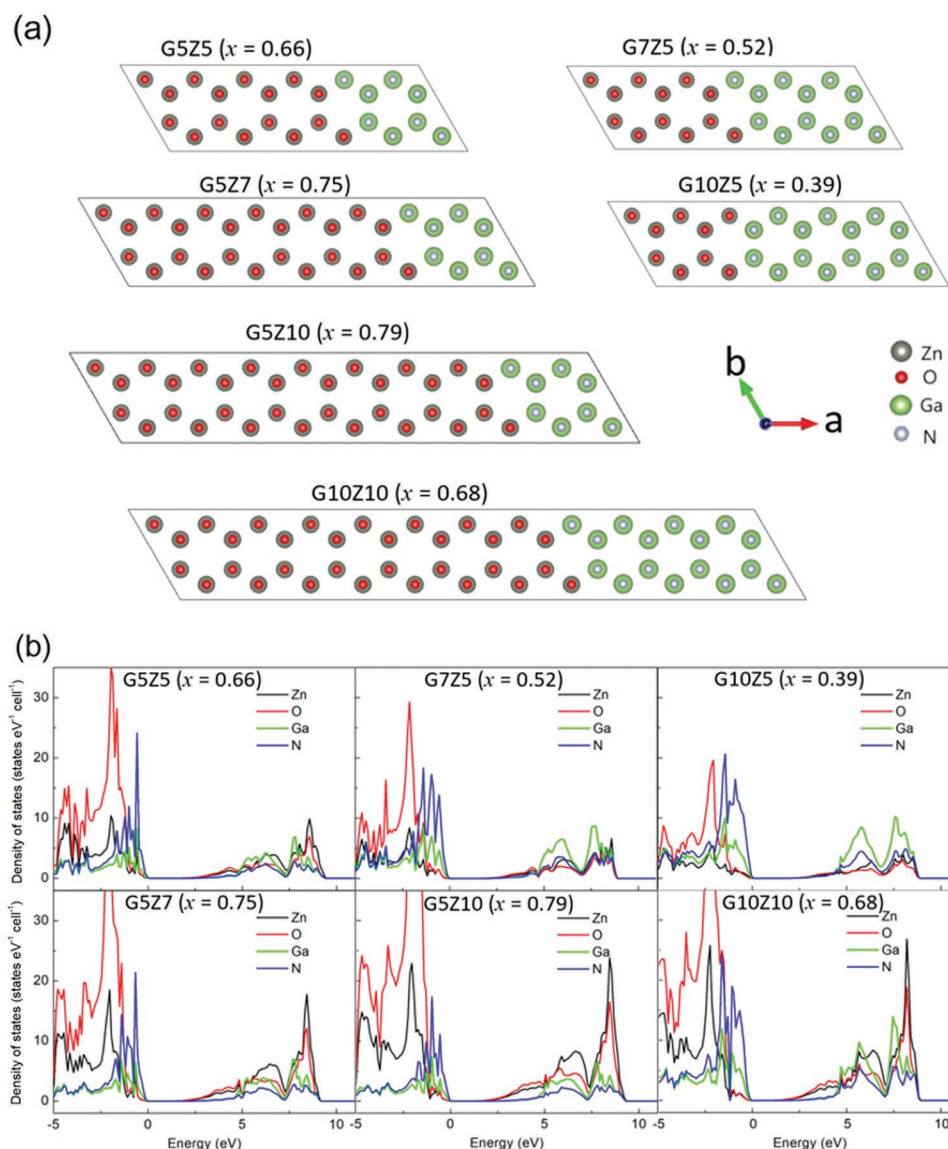


Figure 8. a) Supercell models of all $(\text{GaN})_{1-x}(\text{ZnO})_x$ solid-solution films according to the individual ALD lamination conditions. b) DFT calculations for PDOS projected on the Zn, O, Ga, and N atoms.

calculations) for the GaN, ZnO, and GaN–ZnO solid-solution films are listed in Table 4.

Figure 10a shows the summary of Fermi levels and positions of conduction band and valence band of GaN, ZnO, and $(\text{GaN})_{1-x}(\text{ZnO})_x$ solid-solution films with various values of x . Despite the variation of the Fermi level is relatively small, it basically decreases with increasing the ZnO content. Furthermore, significant band edge shifts are observed in the $(\text{GaN})_{1-x}(\text{ZnO})_x$ samples compared with those of bare GaN and ZnO. It reveals that all of the valence band positions of $(\text{GaN})_{1-x}(\text{ZnO})_x$ are located at more positive potentials than that of bare ZnO, which is attributed to the more contribution of Ga and N atoms in the electron states of valence band based on the calculations of PDOS. On the other hand, all of the conduction band positions of $(\text{GaN})_{1-x}(\text{ZnO})_x$ are very close to that of bare ZnO, that is consistent with the

phenomenon that Zn and O atoms dominate the electron states of conduction band in the above calculations. Consequently, the bandgap reduction of $(\text{GaN})_{1-x}(\text{ZnO})_x$ is mainly attributed to the positive shift of the VBM caused by GaN. It is also noticed that the samples of G10Z5 and G10Z10, both with worse crystallinity, exhibited lower experimental levels of VBM than expected. It may imply that not only the ZnO:GaN ratio but also the crystallinity would affect the band edge positions. In addition, it is worthy of observing the relative band positions in the DFT calculations, as shown in Figure 10b. Despite the calculated band positions may not reflect the real experimental values, the calculated values of DOS show that the positions of CBM and VBM tend to decrease systematically with increasing x .

Figure 11 presents the photocatalytic hydrogen evolution efficiencies of GaN, ZnO, and GaN–ZnO solid-solution

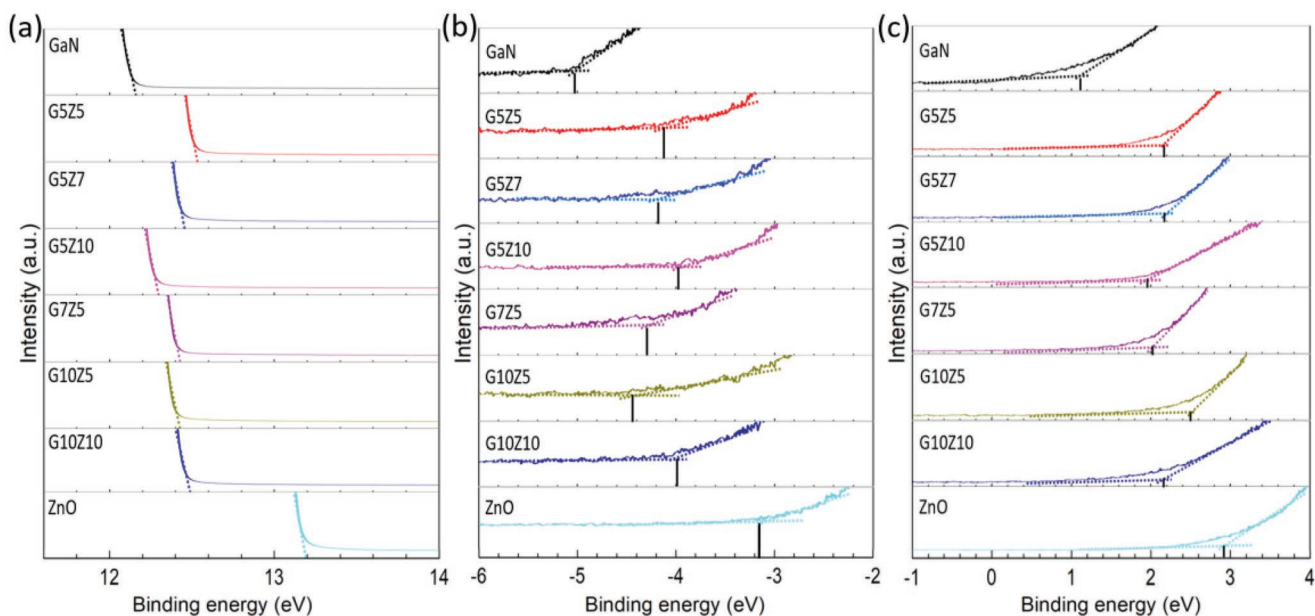


Figure 9. a) UPS (E_{cut}), b) UPS (E_{onset}), and c) UPS-VB (E_{V-F}) spectra for GaN, ZnO, and GaN–ZnO solid-solution films.

films under visible light irradiation. The bare GaN and ZnO exhibit nearly zero hydrogen evolution even after 4 h irradiation due to their large bandgaps. Further, G10Z5 and G10Z10 exhibit very low efficiencies, which may be attributed to their poor crystallinity. By contrast, the other GaN–ZnO solid-solution films reveal significantly improved photocatalytic hydrogen evolution efficiencies. The highest value of $99.1 \mu\text{mol g}^{-1}$ for 4 h was achieved by the G5Z5 sample ($x = 0.66$), and the second highest efficiency was obtained by G7Z5 ($x = 0.52$). It is unexpected that G5Z7 and G5Z10 exhibit relatively low efficiencies of 28.2 and $20.6 \mu\text{mol g}^{-1}$ for 4 h, respectively, despite their lower bandgaps from the DFT calculations. Interestingly, a similar result reported by Dharmagunawardhane et al.^[47] demonstrated that the highest photocatalytic hydrogen evolution of $\approx 23 \mu\text{mol g}^{-1} \text{h}^{-1}$ was obtained for the GaN–ZnO solid solution with 51% ZnO but dramatically dropped to ≈ 0.9 and $\approx 0 \mu\text{mol g}^{-1} \text{h}^{-1}$ for the ones with 76% and 90% ZnO under visible light irradiation.

With the reduction potential of H^+/H_2 and oxidation potential of $\text{O}_2/\text{H}_2\text{O}$, shown in Figure 10a, it is noticed that G7Z5 and G5Z5 possess relatively higher CBM, which could result in a stronger reducing capability of electrons for hydrogen reduction. Although the DFT calculations indicated that a more narrowed bandgap could be obtained by increasing the ZnO content in the solid solution, the above experimental result suggests that the energy levels of conduction band would also be an important factor for enhanced hydrogen evolution.

The present work demonstrates the stacking of multiple alternating layers of GaN/ZnO by ALD lamination to form homogenous solid solutions and DFT calculations to study their PDOS on the Ga, Zn, N, and O for the variation of band structures. These experimental design and numerical analysis provide a promising versatility in manipulating the band structures of GaN–ZnO solid solutions for better photocatalytic hydrogen evolution performance.

Table 4. Summary of UPS data for obtaining work functions and valence band edges of GaN, ZnO, and GaN–ZnO solid solutions. E_{g} is determined by the PDOS of DFT calculations.

Sample	E_{cut} [eV]	E_{onset} [eV]	Φ [eV]	E_{V-F} [eV]	E_{VB} [eV]	E_{g} [eV]
GaN	12.16	−5.03	4.03	1.12	−5.15	3.40
G5Z5	12.53	−4.16	4.53	2.17	−6.70	2.56
G5Z7	12.46	−4.19	4.57	2.18	−6.75	2.34
G5Z10	12.31	−3.99	4.92	1.95	−6.87	2.19
G7Z5	12.43	−4.30	4.49	2.01	−6.50	2.61
G10Z5	12.43	−4.45	4.34	2.50	−6.84	2.67
G10Z10	12.49	−3.99	4.74	2.17	−6.91	2.55
ZnO	13.19	−3.18	4.85	2.91	−7.76	3.20

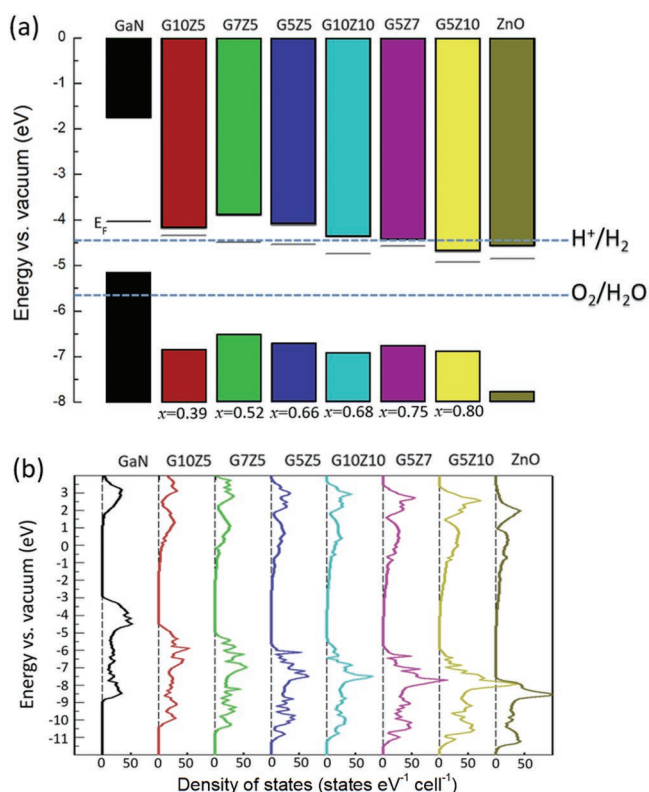


Figure 10. a) Summary of energies of Fermi level, conduction band, and valence band of GaN, ZnO, and $(\text{GaN})_{1-x}(\text{ZnO})_x$ solid-solution films with various values of x and b) corresponding calculated values of DOS from DFT calculations. The reduction potential of H^+/H_2 and oxidation potential of $\text{O}_2/\text{H}_2\text{O}$ are also plotted in (a).

4. Conclusion

GaN–ZnO homogenous solid-solution films were successfully fabricated by ALD nanolamination via varying the cycle ratio

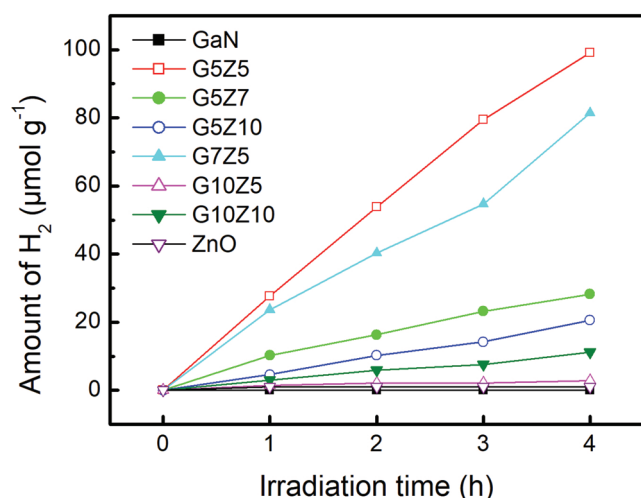


Figure 11. Comparison of visible-light-driven hydrogen evolution efficiencies of GaN, ZnO, and all solid-solution films under 300 W Xe lamp irradiation with a cut-off filter of 420 nm.

of Ga and Zn precursors. The values of x of $(\text{GaN})_{1-x}(\text{ZnO})_x$ in the range of 0.39–0.79 were obtained. A preferred orientation along the (002) was found in bare ZnO, G5Z10, G5Z7, and G10Z10 films but switched to (100) in G5Z5 and G7Z5 films. The growth rates of GaN and ZnO during the ALD lamination process are different from those of pure GaN and ZnO films. GaN grows faster on ZnO, while ZnO grows slower on GaN. Furthermore, the mass density of GaN film is much lower than that of bulk GaN because of the defective structure in the ALD process. The growth rates of GaN and ZnO in each solid-solution films were calibrated, which matched with the experimentally measured thicknesses. The G5Z5 sample was chosen and characterized to be a homogenous solid solution by HRTEM and EDX. Primitive cells of $(\text{GaN})_{1-x}(\text{ZnO})_x$ based on ALD nanolamination were constructed to perform DFT calculations. The PDOS projected on the Zn, O, Ga, and N for various $(\text{GaN})_{1-x}(\text{ZnO})_x$ samples indicate that a higher ratio of ZnO is essential to obtain a higher DOS in the conduction band, resulting in a smaller bandgap. Reduction of the bandgaps to 2.19–2.67 eV was obtained from the calculations. From the UPS analyses and DFT calculations, the VBM and CBM of the $(\text{GaN})_{1-x}(\text{ZnO})_x$ solid solutions exhibit a negative shift as x is increased. The worse crystallinity might also affect the VBM. Visible-light-driven photocatalytic hydrogen evolution was conducted. A significant evolution of $99.1 \mu\text{mol g}^{-1}$ for 4 h was achieved by G5Z5. The different performance for different composition is explained. The present work demonstrates that the stoichiometries of GaN–ZnO films could be controlled with proper calibration of the growth rates of GaN and ZnO, and their band structures could be predicted for better photocatalytic hydrogen evolution performance.

5. Experimental Section

A p-type (100) silicon wafer after ultrasonication cleaning in acetone, isopropanol, and ethanol was used as the substrate for the growth of the GaN–ZnO solid-solution films. Nanolamination of GaN and ZnO layers with various ratios was conducted by a homemade ALD system using TMG ($\text{Ga}(\text{C}_2\text{H}_5)_3$) and DEZ ($\text{Zn}(\text{C}_2\text{H}_5)_2$) as the Ga and Zn precursors, respectively. The substrate temperature was set at 200 °C. For the growth of GaN, the precursor pulse of TMG was 0.5 s, followed by an Ar purge of 7 s. Then an NH_3 plasma of 90 s was employed to form the nitride in a direct plasma reactor by a radio frequency generator (PFG300RF, TRUMPF Hüttinger). For growing ZnO, it started with the pulse of DEZ for 0.3 s, an Ar purge of 7 s, and then a H_2O pulse of 0.1 s. The solid-solution films were obtained by alternating the deposition of GaN and ZnO layers with different repeated cycles. The total number of ALD cycles was fixed at 300 cycles. The bare GaN and ZnO thin films were also prepared with the same cycle number for comparison.

The crystallinity and phases of the as-deposited GaN–ZnO solid-solution thin films were examined by GIXRD (Rigaku TTRAX III) with $\text{Cu K}\alpha$ radiation and a grazing angle of 0.5° . The structures and compositions were further characterized by HRTEM (JEOL JEM-F200) and EDX spectroscopy. The quantitative elemental compositions and work functions were obtained by XPS (ULVAC PHI 5000 Versaprobe II) and UPS (ULVAC PHI 5000 Versaprobe II), respectively. A spectroscopic ellipsometer (Sentech SER800) and XRR (Bruker D8 Discover X-ray) were employed to measure the film thickness and densities. The surface morphologies of the deposited films were characterized using a tapping mode of AFM (Bruker Dimension icon).

DFT calculations using the Vienna ab initio simulation package (VASP) 5.3.5 with Perdew–Burke–Ernzerhof generalized gradient

approximation^[48] were employed to verify the changes of DOS and bandgaps of the GaN–ZnO solid-solution films. The 48-atom supercell models of GaN, ZnO, and GaN–ZnO solid solution were constructed based on the experimental lattice parameters ($a = b = 3.189 \text{ \AA}$ and $c = 5.185 \text{ \AA}$ for the unit cell of GaN,^[49] and $a = b = 3.249 \text{ \AA}$ and $c = 5.206 \text{ \AA}$ for the unit cell of ZnO^[50]). The models were first optimized using a Brillouin zone of $5 \times 2 \times 2$ Monkhorst–Pack k-mesh.^[51] DFT + $U_d + U_p$ method was adopted to obtain the accurate d orbital electronic configuration and DOS, where U_d and U_p are Hubbard correction of d and p orbitals, respectively. The values of U_d applied to both Ga 3d and Zn 3d electrons were set as 10 eV, and the values of U_p for N 2p and O 2p electrons were set as 7.0 and 5.5 eV, respectively.^[52–54] The atomic structure visualization was established by the VESTA program.^[55]

The photocatalytic hydrogen generation efficiency was measured by a gas chromatograph (GC, Shimadzu 2014). A methanol solution (20%) was used as the sacrificial reagent, and a 300-W Xe lamp equipped with a filter ($\lambda \geq 420 \text{ nm}$) was employed as the visible light source. Before the GC analysis, the homemade reactor was purged with Ar to remove the residual gases.

Supporting Information

Supporting Information is available from the Wiley Online Library or from the author.

Acknowledgements

This work was supported by the Ministry of Science and Technology, Taiwan under Contract nos. MOST 107-2221-E-007-006-MY2, MOST 109-2221-E-007-060-MY3, and MOST 109-2112-M-007-034-MY3. The authors also thank supports from National Center for High-performance Computing, Computer and Information Networking Center at National Taiwan University, Academia Sinica Innovative Materials and Analysis Technology Exploration Program (AS-iMATE-109-13), and Center for Quantum Technology at National Tsing Hua University. The authors are also grateful to the assistance by Ching-Wen Tsai, Yi-Jen Yu, and Yen-Ting Liao at the Instrumentation Center, National Tsing Hua University, Kay Yang at the Core Facility Center of National Yang Ming Chiao Tung University, Po-Jung Su at the Core Facility Center of National Cheng Kung University, and Yu-Hsuan Yu and Dr. Chi-Chung Kei at Taiwan Instrument Research Institute.

Conflict of Interest

The authors declare no conflict of interest.

Data Availability Statement

Research data are not shared.

Keywords

atomic layer deposition, density functional theory, GaN, hydrogen evolution, nanolamination, ZnO

Received: August 28, 2022

Revised: November 14, 2022

Published online: January 1, 2023

[1] K. Mazloomi, C. Gomes, *Renewable Sustainable Energy Rev.* **2012**, *16*, 3024.

[2] A. Murphy, P. Barnes, L. Randeniya, I. Plumb, I. Grey, M. Horne, J. Glasscock, *Int. J. Hydrogen Energy* **2006**, *31*, 1999.

- [3] R. Asahi, T. Morikawa, H. Irie, T. Ohwaki, *Chem. Rev.* **2014**, *114*, 9824.
- [4] A. E. Ramirez, M. Montero-Munoz, L. L. Lopez, J. E. Ramos-Ibarra, J. A. H. Coaquira, B. Heinrichs, C. A. Paez, *Sci. Rep.* **2021**, *11*, 2804.
- [5] K. Maeda, T. Takata, M. Hara, N. Saito, Y. Inoue, H. Kobayashi, K. Domen, *J. Am. Chem. Soc.* **2005**, *127*, 8286.
- [6] P. P. Sahoo, P. A. Maggard, *Inorg. Chem.* **2013**, *52*, 4443.
- [7] B. H. Wu, W. T. Liu, T. Y. Chen, T. P. Perng, J. H. Huang, L. J. Chen, *Nano Energy* **2016**, *27*, 412.
- [8] L. Liu, X. Zhang, L. Yang, L. Ren, D. Wang, J. Ye, *Natl. Sci. Rev.* **2017**, *4*, 761.
- [9] Q. Li, H. Meng, P. Zhou, Y. Zheng, J. Wang, J. Yu, J. Gong, *ACS Catal.* **2013**, *3*, 882.
- [10] B. Liu, J. Li, W. Yang, X. Zhang, X. Jiang, Y. Bando, *Small* **2017**, *13*, 1701998.
- [11] W. Yang, B. Liu, B. Yang, J. Wang, T. Sekiguchi, S. Thorsten, X. Jiang, *Adv. Funct. Mater.* **2015**, *25*, 2543.
- [12] J. N. Hart, N. L. Allan, *Adv. Mater.* **2013**, *25*, 2989.
- [13] D. Richards, P. Luce, D. Zemlyanov, A. Ivanisevic, *Scanning* **2012**, *34*, 332.
- [14] K. Maeda, K. Teramura, K. Domen, *J. Catal.* **2008**, *254*, 198.
- [15] K. Maeda, K. Domen, *Chem. Mater.* **2010**, *22*, 612.
- [16] E. J. McDermott, E. Z. Kurmaev, T. D. Boyko, L. D. Finkelstein, R. J. Green, K. Maeda, K. Domen, A. Moewes, *J. Phys. Chem. C* **2012**, *116*, 7694.
- [17] L. L. Jensen, J. T. Muckerman, M. D. Newton, *J. Phys. Chem. C* **2008**, *112*, 3439.
- [18] M. Yoshida, T. Hirai, K. Maeda, N. Saito, J. Kubota, H. Kobayashi, Y. Inoue, K. Domen, *J. Phys. Chem. C* **2010**, *114*, 15510.
- [19] Y. Zhang, D. Q. Fang, S. L. Zhang, R. Huang, Y. H. Wen, *Phys. Chem. Chem. Phys.* **2016**, *18*, 3097.
- [20] P. Tongying, Y. G. Lu, L. M. G. Hall, K. Lee, M. Sulima, J. Ciston, G. Dukovic, *ACS Nano* **2017**, *11*, 8401.
- [21] C. Yang, Y. Hirose, T. Wakasugi, N. Kashiwa, H. Kawai, K. Yamashita, T. Hasegawa, *Phys. Rev. Appl.* **2018**, *10*, 044001.
- [22] S. Göktaş, A. Göktaş, *J. Alloys Compd.* **2021**, *863*, 158734.
- [23] A. Göktaş, *J. Alloys Compd.* **2018**, *735*, 2038.
- [24] K. P. Streubel, W. E. Fenwick, H. Jeon, N. Li, M. Jamil, L. W. Tu, T. Xu, A. Melton, S. Wang, H. Yu, A. Valencia, J. Nause, C. Summers, I. T. Ferguson, *Proc. SPIE* **2009**, *7231*, 723119.
- [25] H. C. Chen, M. J. Chen, M. K. Wu, W. C. Li, H. L. Tsai, J. R. Yang, H. Kuan, M. Shiojiri, *IEEE J. Quantum Electron.* **2010**, *46*, 265.
- [26] E. Guzewicz, I. A. Kowalik, M. Godlewski, K. Kopalko, V. Osinniy, A. Wójcik, S. Yatsunencko, E. Łusakowska, W. Paszkowicz, M. Guzewicz, *J. Appl. Phys.* **2008**, *103*, 033515.
- [27] C. Y. Su, C. C. Wang, Y. C. Hsueh, V. Gurylev, C. C. Kei, T. P. Perng, *Nanoscale* **2015**, *7*, 19222.
- [28] C. Y. Su, C. C. Wang, Y. C. Hsueh, V. Gurylev, C. C. Kei, T. P. Perng, *J. Am. Ceram. Soc.* **2017**, *100*, 4988.
- [29] C. C. Kei, C. C. Wang, T. P. Perng, *J. Am. Ceram. Soc.* **2021**, *104*, 4938.
- [30] X. Chen, H. Baumgart, *Materials* **2020**, *13*, 1283.
- [31] C. Ozgit, I. Donmez, M. Alevli, N. Biyikli, *J. Vac. Sci. Technol., A* **2012**, *30*, 01A124.
- [32] K. Saito, Y. Yamamoto, A. Matsuda, S. Izumi, T. Uchino, K. Ishida, K. Takahashi, *Phys. Status Solidi B* **2002**, *229*, 925.
- [33] G. B. Harris, *Philos. Mag.* **1952**, *43*, 113.
- [34] F. Mikailzade, H. Türkan, F. Önal, Ö. Karataş, S. Kazan, M. Zarbali, A. Göktaş, A. Tumbul, *Appl. Phys. A* **2020**, *126*, 768.
- [35] M. Salah, S. Azizi, A. Boukhachem, C. Khaldi, M. Amlouk, J. Lamloumi, *J. Mater. Sci.* **2017**, *52*, 10439.
- [36] A. A. Gabrienko, S. S. Arzumanov, A. V. Toktarev, I. G. Danilova, I. P. Prosvirin, V. V. Kriventsov, V. I. Zaikovskii, D. Freude, A. G. Stepanov, *ACS Catal.* **2017**, *7*, 1818.
- [37] N. Kaneva, I. Stambolova, V. Blaskov, Y. Dimitriev, S. Vassilev, C. Dushkin, *J. Alloys Compd.* **2010**, *500*, 252.
- [38] R. Huang, F. Li, T. Liu, Y. Zhao, Y. Zhu, Y. Shen, X. Lu, Z. Huang, J. Liu, L. Zhang, S. Zhang, Z. Li, A. Dingsun, H. Yang, *Sci. Rep.* **2018**, *8*, 8521.

- [39] S. K. Nayak, M. Gupta, S. M. Shivaprasad, *RSC Adv.* **2017**, *7*, 25998.
- [40] R. A. Fischer, A. Wohlfart, A. Devi, W. Rogge, *MRS Internet J. Nitride Semicond. Res.* **2000**, *5*, 152.
- [41] A. G. Shard, *J. Vac. Sci. Technol., A* **2020**, *38*, 041201.
- [42] H. J. Yun, H. Kim, B. J. Choi, *Ceram. Int.* **2020**, *46*, 13372.
- [43] V. I. Anisimov, J. Zaanen, O. K. Andersen, *Phys. Rev. B* **1991**, *44*, 943.
- [44] Y. Li, L. Zhu, Y. Yang, H. Song, Z. Lou, Y. Guo, Z. Ye, *Small* **2015**, *11*, 871.
- [45] W. Q. Han, Z. Liu, H. G. Yu, *Appl. Phys. Lett.* **2010**, *96*, 183112.
- [46] Ü. Özgür, Y. I. Alivov, C. Liu, A. Teke, M. A. Reshchikov, S. Doğan, V. Avrutin, S. J. Cho, H. Morkoç, *J. Appl. Phys.* **2005**, *98*, 041301.
- [47] H. A. N. Dharmagunawardhane, A. James, Q. Wu, W. R. Woerner, R. M. Palomino, A. Sinclair, A. Orlov, J. B. Parise, *RSC Adv.* **2018**, *8*, 8976.
- [48] J. P. Perdew, K. Burke, M. Ernzerhof, *Phys. Rev. Lett.* **1996**, *77*, 3865.
- [49] H. Qin, X. Luan, C. Feng, D. Yang, G. Zhang, *Materials* **2017**, *10*, 1419.
- [50] R. D. Vispute, V. Talyansky, S. Choo-pun, R. P. Sharma, T. Venkatesan, M. He, X. Tang, J. B. Halpern, M. G. Spencer, Y. X. Li, L. G. Salamanca-Riba, A. A. Iliadis, K. A. Jones, *Appl. Phys. Lett.* **1998**, *73*, 348.
- [51] H. J. Monkhorst, J. D. Pack, *Phys. Rev. B* **1976**, *13*, 5188.
- [52] Y. S. Lee, Y. C. Peng, J. H. Lu, Y. R. Zhu, H. C. Wu, *Thin Solid Films* **2014**, *570*, 464.
- [53] O. Bovgyra, M. Kovalenko, V. Y. Dzikovskyi, A. Vaskiv, M. Y. Sheremeta, *J. Nano- Electron. Phys.* **2020**, *12*, 05003.
- [54] K. Harun, N. A. Salleh, B. Deghfel, M. K. Yaakob, A. A. Mohamad, *Results Phys.* **2020**, *16*, 102829.
- [55] K. Momma, F. Izumi, *J. Appl. Crystallogr.* **2011**, *44*, 1272.